Spatial light interference tomography (SLIT)

Zhuo Wang[1,2], Daniel L. Marks[1,2], Paul Scott Carney[1,2], Larry J. Millet[3], Martha U. Gillette[3], Agustin Mihi[2,4], Paul V. Braun[2,4], Zhen Shen[3], Supriya G. Prasanth[3], and Gabriel Popescu[1,2,*]

[1]*Department of Electrical and Computer Engineering, University of Illinois at Urbana-Champaign, Urbana, IL 61801, USA*
[2]*Beckman Institute for Advanced Science & Technology, University of Illinois at Urbana-Champaign, Urbana, IL 61801, USA*
[3]*Department of Cell and Developmental Biology, University of Illinois at Urbana-Champaign, Urbana, Illinois 61801, USA*
[4]*Department of Material Science and Engineering, University of Illinois at Urbana-Champaign, Urbana, Illinois 61801, USA*
*gpopescu@illinois.edu

Abstract: We present spatial light interference tomography (SLIT), a label-free method for 3D imaging of transparent structures such as live cells. SLIT uses the principle of interferometric imaging with broadband fields and combines the optical gating due to the micron-scale coherence length with that of the high numerical aperture objective lens. Measuring the phase shift map associated with the object as it is translated through focus provides full information about the 3D distribution associated with the refractive index. Using a reconstruction algorithm based on the Born approximation, we show that the sample structure may be recovered via a 3D, complex field deconvolution. We illustrate the method with reconstructed tomographic refractive index distributions of microspheres, photonic crystals, and unstained living cells.

OCIS Codes: (180.6900) Three-dimensional microscopy; (290.3200) Inverse scattering; (999.9999) Quantitative phase imaging

Referenes

1. J. B. Pawley, *Handbook of biological confocal microscopy* (Springer, New York, 2006).
2. J. G. McNally, T. Karpova, J. Cooper, and J. A. Conchello, "Three-dimensional imaging by deconvolution microscopy," Methods **19**(3), 373–385 (1999).
3. G. E. Bacon, *X-ray and neutron diffraction* (Pergamon, 1966).
4. J. D. Watson and F. H. C. Crick, "Molecular structure of nucleic acids; a structure for deoxyribose nucleic acid," Nature **171**(4356), 737–738 (1953).
5. N. Ban, P. Nissen, J. Hansen, P. B. Moore, and T. A. Steitz, "The complete atomic structure of the large ribosomal subunit at 2.4 A resolution," Science **289**(5481), 905–920 (2000).
6. E. Wolf, "History and Solution of the Phase Problem in the Theory of Structure Determination of Crystals from X-Ray Diffraction Measurements," in *Advances in Imaging and electron physics*, P. W. E. Hawkes, ed. (Academic Press, San Diego, 2011).
7. D. Gabor, "A new microscopic principle," Nature **161**(4098), 777–778 (1948).
8. P. Hariharan, *Basics of holography* (Cambridge University Press, Cambridge, UK; New York, NY, 2002).
9. E. Wolf, "Three-dimensional structure determination of semi-transparent objects from holographic data," Opt. Commun. **1**(4), 153–156 (1969).
10. M. Debailleul, V. Georges, B. Simon, R. Morin, and O. Haeberlé, "High-resolution three-dimensional tomographic diffractive microscopy of transparent inorganic and biological samples," Opt. Lett. **34**(1), 79–81 (2009).
11. G. N. Vishnyakov, G. G. Levin, V. L. Minaev, V. V. Pickalov, and A. V. Likhachev, "Tomographic Interference Microscopy of Living Cells," Microscopy and Analysis **18**, 15–17 (2004).
12. F. Montfort, T. Colomb, F. Charrière, J. Kühn, P. Marquet, E. Cuche, S. Herminjard, and C. Depeursinge, "Submicrometer optical tomography by multiple-wavelength digital holographic microscopy," Appl. Opt. **45**(32), 8209–8217 (2006).

13. J. Kühn, F. Montfort, T. Colomb, B. Rappaz, C. Moratal, N. Pavillon, P. Marquet, and C. Depeursinge, "Submicrometer tomography of cells by multiple-wavelength digital holographic microscopy in reflection," Opt. Lett. **34**(5), 653–655 (2009).
14. D. Hillmann, C. Lührs, T. Bonin, P. Koch, and G. Hüttmann, "Holoscopy--holographic optical coherence tomography," Opt. Lett. **36**(13), 2390–2392 (2011).
15. F. Charrière, A. Marian, T. Colomb, P. Marquet, and C. Depeursinge, "Amplitude point-spread function measurement of high-NA microscope objectives by digital holographic microscopy," Opt. Lett. **32**(16), 2456–2458 (2007).
16. A. Marian, F. Charrière, T. Colomb, F. Montfort, J. Kühn, P. Marquet, and C. Depeursinge, "On the complex three-dimensional amplitude point spread function of lenses and microscope objectives: theoretical aspects, simulations and measurements by digital holography," J. Microsc. **225**(Pt 2), 156–169 (2007).
17. H. Ding and G. Popescu, "Coherent light imaging and scattering for biological investigations," in *Coherent light microscopy*, P. Ferraro, A. Wax, and Z. Zalevsky, eds. (Springer, Berlin Heidelberg, 2011), pp. 229–265.
18. G. Popescu, "Quantitative phase imaging of nanoscale cell structure and dynamics," in *Methods in Cell Biology*, P. J. Bhanu, ed. (Elsevier, 2008), p. 87.
19. C. Depeursinge, "Digital Holography Applied to Microscopy " in *Digital Holography and Three-Dimensional Display*, T.-C. Poon, ed. (Springer US, 2006), p. 98.
20. B. Q. Chen and J. J. Stamnes, "Validity of diffraction tomography based on the first born and the first rytov approximations," Appl. Opt. **37**(14), 2996–3006 (1998).
21. G. Gbur and E. Wolf, "Relation between computed tomography and diffraction tomography," J. Opt. Soc. Am. A **18**(9), 2132–2137 (2001).
22. P. S. Carney, E. Wolf, and G. S. Agarwal, "Diffraction tomography using power extinction measurements," J. Opt. Soc. Am. A **16**(11), 2643–2648 (1999).
23. V. Lauer, "New approach to optical diffraction tomography yielding a vector equation of diffraction tomography and a novel tomographic microscope," J. Microsc. **205**(Pt 2), 165–176 (2002).
24. A. M. Zysk, J. J. Reynolds, D. L. Marks, P. S. Carney, and S. A. Boppart, "Projected index computed tomography," Opt. Lett. **28**(9), 701–703 (2003).
25. F. Charrière, N. Pavillon, T. Colomb, C. Depeursinge, T. J. Heger, E. A. D. Mitchell, P. Marquet, and B. Rappaz, "Living specimen tomography by digital holographic microscopy: morphometry of testate amoeba," Opt. Express **14**(16), 7005–7013 (2006).
26. F. Charrière, A. Marian, F. Montfort, J. Kuehn, T. Colomb, E. Cuche, P. Marquet, and C. Depeursinge, "Cell refractive index tomography by digital holographic microscopy," Opt. Lett. **31**(2), 178–180 (2006).
27. W. Choi, C. Fang-Yen, K. Badizadegan, S. Oh, N. Lue, R. R. Dasari, and M. S. Feld, "Tomographic phase microscopy," Nat. Methods **4**(9), 717–719 (2007).
28. W. S. Choi, C. Fang-Yen, K. Badizadegan, R. R. Dasari, and M. S. Feld, "Extended depth of focus in tomographic phase microscopy using a propagation algorithm," Opt. Lett. **33**(2), 171–173 (2008).
29. Z. Wang, L. J. Millet, M. Mir, H. Ding, S. Unarunotai, J. A. Rogers, M. U. Gillette, and G. Popescu, "Spatial light interference microscopy (SLIM)," Opt. Express **19**(2), 1016–1026 (2011).
30. Z. Wang and G. Popescu, "Quantitative phase imaging with broadband fields," Appl. Phys. Lett. **96**(5), 051117 (2010).
31. M. Born and E. Wolf, *Principles of optics: electromagnetic theory of propagation, interference and diffraction of light* (Cambridge University Press, Cambridge; New York, 1999).
32. R. P. Dougherty, "Extensions of DAMAS and Benefits and Limitations of Deconvolution in Beamforming," 11th AIAA/CEAS Aeroacoustics Conference (26th AIAA Aeroacoustics Conference) **AIAA**, 2005–2961 (2005).
33. P. A. Midgley and M. Weyland, "3D electron microscopy in the physical sciences: the development of Z-contrast and EFTEM tomography," Ultramicroscopy **96**(3-4), 413–431 (2003).
34. F. Zernike, "How I discovered phase contrast," Science **121**(3141), 345–349 (1955).
35. N. Lue, G. Popescu, T. Ikeda, R. R. Dasari, K. Badizadegan, and M. S. Feld, "Live cell refractometry using microfluidic devices," Opt. Lett. **31**(18), 2759–2761 (2006).
36. B. Lillis, M. Manning, H. Berney, E. Hurley, A. Mathewson, and M. M. Sheehan, "Dual polarisation interferometry characterisation of DNA immobilisation and hybridisation detection on a silanised support," Biosens. Bioelectron. **21**(8), 1459–1467 (2006).
37. D. Huang, E. A. Swanson, C. P. Lin, J. S. Schuman, W. G. Stinson, W. Chang, M. R. Hee, T. Flotte, K. Gregory, C. A. Puliafito, and J. G. Fujimoto, "Optical coherence tomography," Science **254**(5035), 1178–1181 (1991).
38. G. Popescu, Y. Park, N. Lue, C. Best-Popescu, L. Deflores, R. R. Dasari, M. S. Feld, and K. Badizadegan, "Optical imaging of cell mass and growth dynamics," Am. J. Physiol. Cell Physiol. **295**(2), C538–C544 (2008).
39. H. F. Ding and G. Popescu, "Instantaneous spatial light interference microscopy," Opt. Express **18**(2), 1569–1575 (2010).
40. L. J. Millet, M. E. Stewart, J. V. Sweedler, R. G. Nuzzo, and M. U. Gillette, "Microfluidic devices for culturing primary mammalian neurons at low densities," Lab Chip **7**(8), 987–994 (2007).

1. Introduction

3D optical imaging of cells has been dominated by fluorescence *confocal microscopy*, where the specimen is typically fixed and tagged with exogenous fluorophores [1]. The image is

rendered serially, i.e., point by point, and the out-of-focus light is rejected by a pinhole in front of the detector. Alternatively, the three-dimensional (3D) structure can be obtained via *deconvolution microscopy*, in which a series of fluorescence images along the optical axis of the system is recorded instead [2]. The deconvolution numerically reassigns the out-of-focus light, instead of removing it, thus making better use of the available signal at the expense of increased computation time. Label-free methods are preferable especially when photobleaching and phototoxicity play a limiting role. It has been known since the work by von Laue and the Braggs that the structure of 3D, *weakly scattering* media, can be determined by *far-zone* measurements of scattered electromagnetic fields [3]. In biology, X-ray and electron scattering by crystalline matter enabled momentous discoveries, from the structure of the DNA molecule [4] to that of the ribosome [5]. Despite the great success of methods based on scattering and analysis, they suffered from the so-called "phase problem" (for a recent review of the subject, see Ref [6].). Essentially, reconstructing a 3D structure from measurements of scattered fields, i.e., solving the *inverse scattering problem*, requires that both the amplitude and phase of the field are measured. The scattered fields are uniquely related to the structure of the object, but a given intensity may be produced by many fields, each corresponding to a different sample structure. This nonuniqueness inherent in intensity measurements may be overcome by prior assumptions and within certain approximations, e.g. see Ref [6].

In the optical regime, interferometric experiments from which the complex scattered field may be inferred are practicable. The prime example is Gabor's holography1940's [7] though many refinements and variations have been developed since [8]. Holographic data obtained from many view angles are sufficient for the unambiguous reconstruction of the sample. Such solution of the so-called inverse scattering problem with light was presented by Wolf and the approach became known as *diffraction tomography* [9]. Recently, a number of papers have reported various approaches for 3D reconstructions of transparent objects [10–16].

Here we present SLIT, a new *label-free* method for 3D tomographic imaging of transparent structures. The main challenge in imaging unlabelled live cells stems from their transparency, resulting in weak scattered fields and behaviour as phase objects [17]. The phase introduced by the object appears in the signal as an additional delay or optical pathlength. Thus, *quantifying* optical path-lengths permits label-free measurements of structures and motions in a non-contact, non-invasive manner. Quantitative phase imaging (QPI) has recently become an active field of study and various experimental approaches have been proposed and demonstrated [18,19]. Radon-transform-based reconstruction algorithms together with phase-sensitive measurements have enabled optical tomography of transparent structures [20–24]. More recently, this type of QPI-based projection tomography has been applied to live cells [25–27]. However, the approximation used in this computed tomography fails for high numerical aperture imaging, where diffraction effects are significant and limit the depth of field that can be reconstructed reliably [28].

SLIT brings together broad-band interferometry [29,30] and high-resolution imaging. Combining white light illumination, high numerical aperture imaging, and phase-resolved detection, SLIT renders inhomogeneous three-dimensional distributions of refractive index. Based on the first order Born approximation (see for example, Chapter 13 in Ref [31].), we developed a model that relates the measured optical field to a 3D convolution operation of the susceptibility and the instrument response. From the complex-field deconvolution, we extracted the 3D refractive index distribution of transparent specimens, including photonic crystals and live cells.

2. Results

2.1 SLIT depth sectioning through live cells

In order to obtain a tomographic image of a sample, we perform axial scanning by translating the sample through focus in step sizes of less than half the Rayleigh range, with an accuracy of 20 nm. At each axial position, we record a quantitative phase image using the principle of spatial light interference microscopy (SLIM), described in more detail elsewhere [29]. In SLIM, the image is considered an interferogram between the scattered and unscattered fields. Shifting the relative phase between these two fields in 4 successive steps of π/2 and recording the 4 corresponding images, we can quantitatively extract the pathlength map associated with the specimen with sub-nanometer sensitivity. In order to obtain a tomographic image of a sample, we translate the sample through focus in step sizes of less than half the depth of field with an accuracy of 20 nm. The tomographic capability of this imaging system can understood as follows.

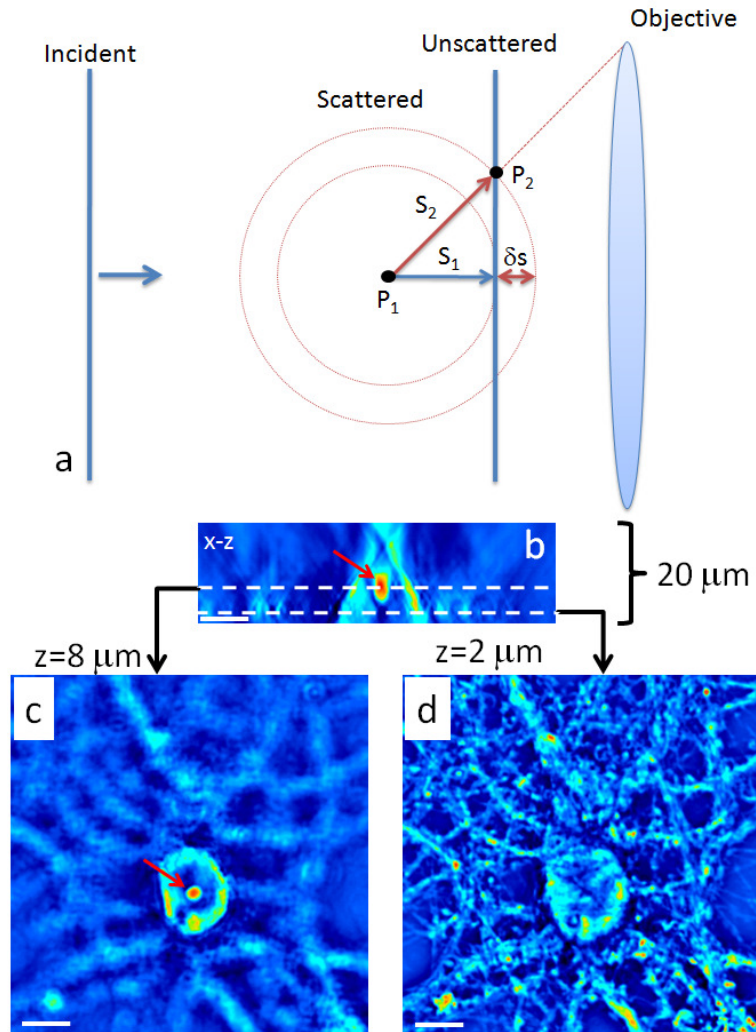Fig. 1. Visualization of 3D sectioning of SLIM. (**a**) Sectioning effect of SLIM with coherence gating. (**b**) An x-z cut through a live neuron; the bottom of the image corresponds to the glass surface. The soma and nucleolus (arrow) are clearly visible. (**c-d**) Images of the same neuron at the depths indicated by the dash lines in (**b**). Scale bar for (b-d): 10 μm.

Figures 1b-d illustrate this approach with quantitative phase images obtained on a live neuron. While there is certain elongation in the z-axis, as indicated especially by the shape of the cell body in Fig. 1b, it is evident that SLIM provides optical sectioning without further processing. Specifically, at the substrate plane (z = 2 μm) the neuronal processes are clearly in focus and the nucleolus is absent. However, 6 μm above this plane, the cell body and nucleolus are clearly in focus, while the contributions from the processes are subdominant. Starting with these quantitative phase images, we solve the inverse scattering problem, as detailed below.
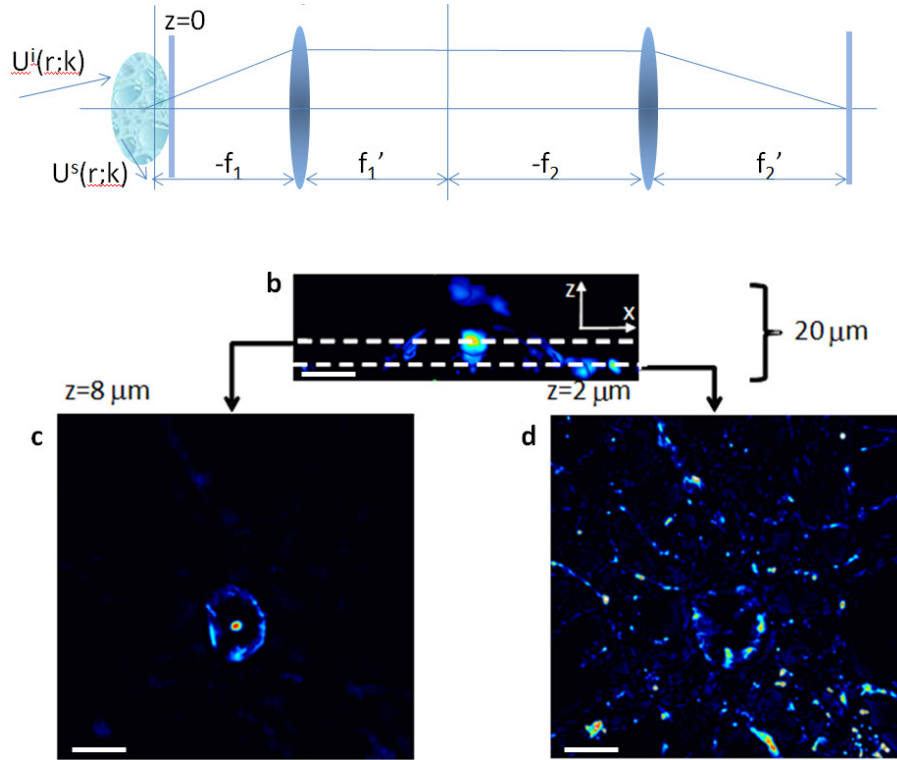
2.2 Tomographic reconstruction

Fig. 2. SLIT based on scattering theory. (a) Schematic plot for 3D reconstruction. (b-d) Counterparts of Fig. 1 b-d after 3D reconstruction. Scale bar for (b-d): 10 μm.

The scattering problem can be formulated as follows (see Fig. 2a). Consider a plane wave incident on the specimen, which becomes a secondary field source. The fields scattered from each point within the sample propagate as spherical waves such that the unscattered plane wave interferes with the scattered field. The imaging system behaves as a band pass filter in the wave vector space (**k**) and collects these fields at the detector. Tomography is made tractable by a linear forward model which is the essence of the first Born approximation of (weak) scattering used here. The linearity assumed here is consistent with diffraction tomography, as described by Wolf in 1969 [9].

Thus, at each optical frequency, the 3D field distribution $U(x, y, z)$, measured via depth scanning, is the result of the convolution between the susceptibility of the specimen and the point spread function, P, of the microscope,

$$U(\mathbf{r}) = \iiint_V \chi(\mathbf{r'})P(\mathbf{r} - \mathbf{r'})d^3\mathbf{r'}, \tag{1}$$

where $\chi(\mathbf{r}) = n^2(\mathbf{r}) - 1$ is the spatial component of the susceptibility, assumed to be dispersion-free, and represents the quantity of interest in our reconstruction. Note that U here represents the real part (cosine component) of the complex analytic signal measured experimentally. Let $\tilde{U}(\mathbf{q})$, $\tilde{\chi}(\mathbf{q})$ and $\tilde{P}(\mathbf{q})$ be the Fourier transforms of U, χ, and P, respectively, such that Eq. (1) can be written in the frequency domain $\mathbf{q}$ as

$$\tilde{U}(\mathbf{q}) = \tilde{\chi}(\mathbf{q})\tilde{P}(\mathbf{q}), \tag{2}$$

where ~indicates Fourier transformation. Thus, the Fourier transform of the susceptibility can be obtained as the ratio between the Fourier transform of the measured field and that of the instrument function,

$$\tilde{\chi}(\mathbf{q}) = \tilde{U}(\mathbf{q}) / \tilde{P}(\mathbf{q}), \tag{3}$$

In order to perform the deconvolution in Eq. (3), one requires the knowledge of P as a function of all 3 coordinates. In principle, P can be modelled by analysing all of the optical components. However, a complete description of the imaging system, is challenging. Therefore, we obtain P experimentally instead. We imaged microspheres with diameters of approximately one-third of the diffraction spot, effectively representing point scatterers. We measured the point spread function by scanning through focus a 200 nm diameter polystyrene bead for 40 × /0.75 objectives (50 nm for 63 × /1.4 objective). Phase and amplitude images were measured at each depth, incremented in steps of 200 nm, and function P was obtained as the real part of this measured complex analytic signal. The measured P is shown in Fig. 3. The full-width-half-maximum of $P(x)$ has a value of 0.36 µm. The-full-width-half-maximum of the $P(z)$ main lobe, which defines the axial resolution, has a value $\delta z = 1.34$ µm.

The point spread function P has finite frequency support, which makes the ratio $\tilde{\chi}(\mathbf{q}) = \tilde{U}(\mathbf{q}) / \tilde{P}(\mathbf{q})$ diverge in certain domains. Therefore, suitable regularization is required. We used the conventional Wiener deconvolution procedure and followed the implementation by Dougherty [32], as detailed in Appendix. To illustrate the procedure, the reconstructed 3D refractive index map associated with the neuron in Figs. 1b-d is shown in Fig. 2b-d. It can be seen, that unlike in the raw phase images (Figs. 1b-d), in the reconstructed images, most out-of-focus light is rejected after reconstruction.
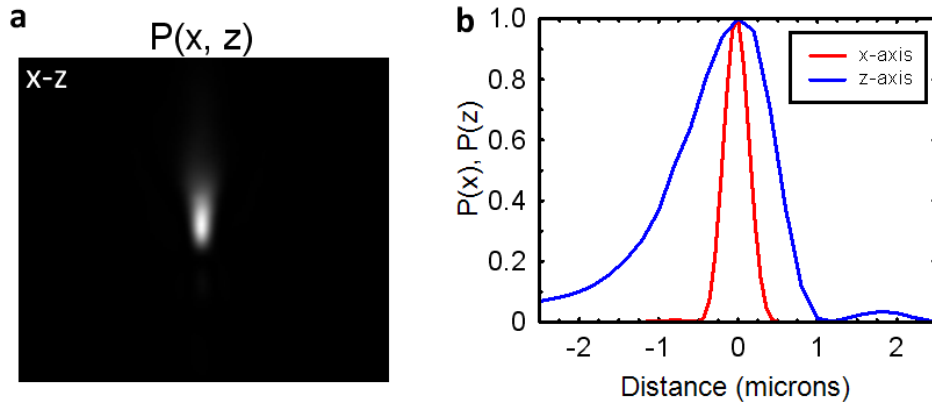

Fig. 3. Measured point spread function (PSF). Objective: Zeiss EC Plan-Neofluar 40 × /0.75. **a,** The PSF in the x-z plane. **b,** PSF profiles along x- and z-axis.

2.3 SLIT of standard samples

We also measured beads (Polyscience Inc., diameter 3.12 μm) immersed in microscope immersion oil (Zeiss Immersol 518F, refractive index 1.518). Figure 4 shows the reconstructed phase map of different z positions. A defect within the bead (apparently a pore) is clearly seen at the z = −1.45 μm slice.

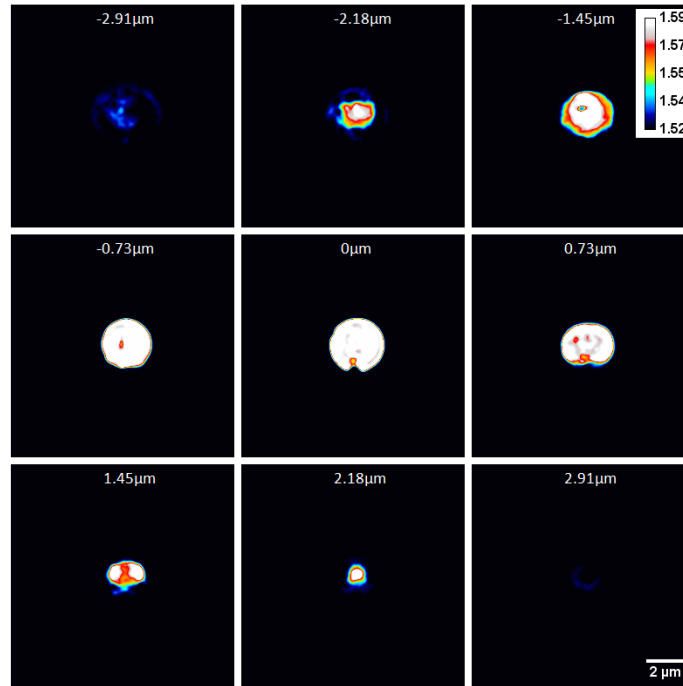Fig. 4. Refractive index map of 3.1 μm polystyrene beads in immersion oil (Zeiss Immersol 518F, refractive index 1.518) at different Z positions. Objective: Zeiss Plan-Apochromatic 63 × /1.4 oil.

Also a cleaved edge of the beads can be found at z = 0 μm. Supplementary Movie 1 shows the complete depth sectioning of the same bead. The bead is elongated along z direction because of the missing collection angle due to the finite NA of the objective [33]. Current effort in our lab is devoted toward a better frequency coverage to improve the z-resolution and eliminate the elongation.

SLIT also may be a useful tool for imaging nonbiological structures such as photonics crystals, for which the refractive index is difficult to access experimentally. We applied SLIT to photonic crystal samples that are obtained from 1 μm SiO2 spheres (Fiber Optic Center Inc.) dispersed in ethanol (4% w/w, see Fig. 5). Approximately 6 ml of microsphere suspension was dispensed into a 20 ml scintillation vial (Fisher) with a 1 cm × 2.5 cm cut glass coverslip. The substrate was placed at an angle (about 35°) in the vial. The temperature was set to 50 °C in an incubator (Fisher, Isotemp 125D). The sample is immersed in alcohol and covered with another coverslip upon imaging. As evident in Fig. 5, it is difficult to indentify three consecutive layers of 1 μm silica beads via axial scanning with phase contrast microscopy. The SLIM (i.e., quantitative phase) images show clear sectioning, though out-of-focus light still persists.

However, the sectioning is further improved with our deconvolution algorithm, as shown in the SLIT images, where most of the out-of-focus light is rejected. The notorious halo effect associated with phase contrast images is clearly visible [34]. Due to our phase shifting image reconstruction, this effect is significantly diminished in the SLIM images, but still observable.

The tomographic reconstruction is also affected, especially in areas highlighted by the halo in the phase contrast images.
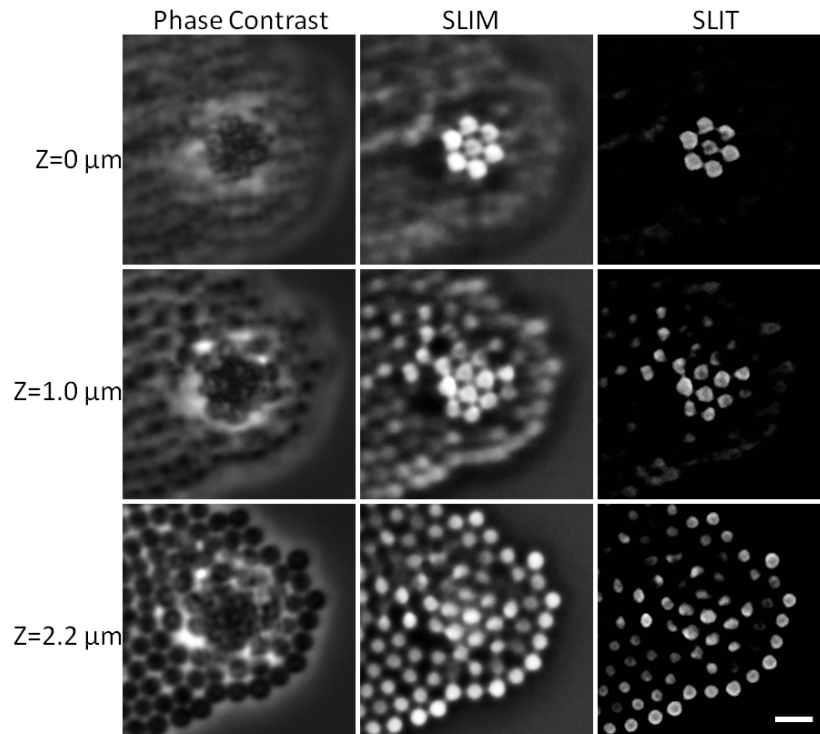

Fig. 5. Comparison of sectioning effect in phase contrast, SLIM and SLIT measurement of the same photonic crystal samples. The sample is made by 1 μm silica beads index matched with isopropyl alcohol (IPA). Scale bar: 2 μm. Objective: Zeiss Plan-Apochromat 63 × /1.4 oil.

2.4 Label-free live cell tomography

Perhaps one of the most appealing applications of SLIT is the 3D imaging of live, unstained cells. We performed SLIM experiments on live neuron cultures. Results obtained from a single neuron are shown in Fig. 6. Thus, Figs. 6a-b show two sections separated by 5.6 μm. Notably, for some regions of the cytoplasm, the refractive index distribution is below 1.39, which is compatible with previous average refractive index measurements on other cell types [35].
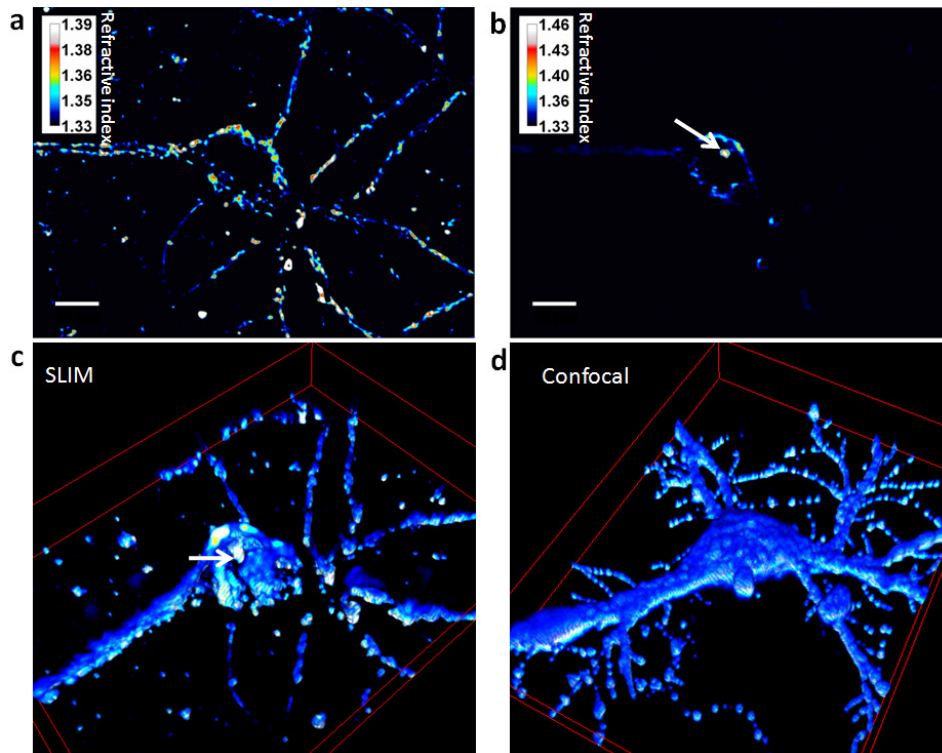
Fig. 6. Tomography capability. (**a**)-(**b**) Refractive index distribution through a live neuron at position z = 0.4 μm (**a**) and 6.0 μm (**b**). The soma and nucleolus (arrow) are clearly visible. Scale bars, 10 μm. (**c**) 3D rendering of the same cell. The field of view is 100 μm × 75 μm × 14 μm and NA = 0.75. (**d**) confocal microscopy of a stained neuron with same field of view and NA = 1.2. Neurons were labeled with anti-polysialic acid IgG #735. The 3D rendering in (**c**) and (**d**) was done by ImageJ 3D viewer.

The nucleolus (arrow, Fig. 6b) has a higher value, n~1.46, which agrees with previous measurements on DNA [36]. Figure 6c shows a 3D rendering of the same hippocampal neuron generated from 71 images separated by 14 μm. For comparison, we used fluorescence confocal microscopy to obtain a similar view of a different hippocampal neuron cultured under identical conditions (Fig. 6d). This neuron was stained with anti-polysialic acid IgG #735 An animated side-by-side comparison of the two 3D renderings and the corresponding z stacks used to generate them are shown in Supplementary Movies 2, 3 and 4, respectively. The numerical aperture of the confocal microscope objective was NA = 1.2, which is higher than that used in SLIT (NA = 0.75), which explains the higher resolution of the confocal image. Nevertheless the 3D imaging by SLIT is qualitatively similar to that obtained by fluorescence confocal microscopy. However, in contrast to confocal microscopy, SLIT is label-free and enables non-invasive imaging of living cells over long periods of time, with substantially lower illumination power density. The typical irradiance at the sample plane is ~1 nW/μm^2. The exposure time was 10-50 ms for all the images presented in the manuscript. This level of exposure is 6-7 orders of magnitude less than that of typical confocal microscopy and, therefore, reduces photoxicity during extended live-cell imaging. The high refractive index associated with segregating chromosomes allows their imaging with high contrast during cell mitosis (Supplementary Movie 5). This type of 4D (x,y,z, time) imaging may yield new insights into cell division, motility, differentiation, and growth. Current work is devoted in our laboratory to reduce the z-axis elongation via better frequency coverage and improve the reconstruction of cell membranes, via higher sensitivity measurements.

3. Summary and discussion

The combination of low-coherence light illumination and shallow depth of field, allows SLIT to render 3D tomographic images of transparent structures. The optical gating due to the low-coherence of light is at the heart of optical coherence tomography, which is now a well-established method for deep tissue imaging [37]. Note that in SLIT the optical sectioning ability depends also on the numerical aperture of the objective, i.e. *depth of field gating*. SLIT provides stronger depth sectioning at higher numerical aperture because both the reference and the object beams are traveling through the sample. This aspect adds important versatility to SLIT, as it can adapt from low NA imaging when no sectioning is needed and, instead, the phase integral through the entire object thickness is obtained (e.g., cell dry mass measurements [38]) to high NA imaging, when only a thin slice through the object is of interest. Of course, the two optical gates (coherence and depth of field) inherently overlap axially because the two interfering fields are derived from the same image field. Further discussion for the adjustable optical sectioning of SLIM can be found in Appendix. The current acquisition rate allows for a typical tomogram to be acquired in less than a minute. However, this is not a limitation of principle and can be improved by using faster QPI methods (e.g. as in Ref [39].).

Our results demonstrate that rich quantitative information can be captured from both fixed structures and cells using SLIT. In essence, SLIT combines microscopy and interferometry to solve the *inverse scattering* problem. Because of its implementation with existing phase contrast microscopes, SLIT has the potential to make a broad impact and elevate phase-based imaging from *observing* to *quantifying* over a broad range of spatiotemporal scales. We anticipate that the studies allowed by SLIT will further our understanding of basic phenomena related to biological applications as well as material science research.

Appendix

A.1 Deconvolution algorithm

Here we provide a detailed mathematical description of SLIT 3D reconstruction based on the DAMAS [32] iterative deconvolution.

For a transparent sample such as a live cell, the 3D complex field measured U is the result of the convolution between the electrical susceptibility of the specimen and the PSF of the microscope,

$$U(\mathbf{r}) = \chi(\mathbf{r}) \underset{3D}{\odot} P(\mathbf{r}), \qquad (4)$$

where $\chi(\mathbf{r}) = n^2(\mathbf{r}) - 1$ the susceptibility and $\underset{3D}{\odot}$ the 3D spatial deconvolution. $\tilde{U}(\mathbf{k})$, $\tilde{\chi}(\mathbf{k})$ and $\tilde{P}(\mathbf{k})$ represent the FFT of $U(\mathbf{r})$, $\chi(\mathbf{r})$ and $P(\mathbf{r})$. In order to reduce the number of iterations needed for convergence, a regularized division of *PSF* and *U* by the FFT of the *PSF* in the spectral domain are performed, which gives the modified deconvolution problem

$$U_w(\mathbf{r}) = \chi(\mathbf{r}) \underset{3D}{\odot} P_w(\mathbf{r}), \qquad (5)$$

A non-negative solution is then sought by iteration. The aforementioned algorithm can be expressed as follows:

Compute the forward FFT of *U* and *P*;

For each frequency $\mathbf{k}$, computer $\tilde{U}_w(\mathbf{k}) = \dfrac{\tilde{P}^*(\mathbf{k})\tilde{U}(\mathbf{k})}{\tilde{P}^*(\mathbf{k})\tilde{P}(\mathbf{k}) + \gamma}$ and

$$\tilde{P}_w(\mathbf{k}) = \frac{\tilde{P}^*(\mathbf{k})\tilde{P}(\mathbf{k})}{\tilde{P}^*(\mathbf{k})\tilde{P}(\mathbf{k}) + \gamma};$$

Compute the inverse FFT of $\tilde{P}_w(\mathbf{k})$ to obtain P_w;

Set $a = \sum_{x,y,z} P_w;$

Set solution $\chi(\mathbf{r}) = 0$;

Iterate

(1) $\tilde{\chi}(\mathbf{k})$ = forward FFT of [χ];

(2) Let $\tilde{R}(\mathbf{k}) = \tilde{P}_w(\mathbf{k})\tilde{\chi}(\mathbf{k});$

(3) $R(\mathbf{r}) = $ inverse FFT of [$\tilde{R}(\mathbf{k})$];

(4) $\chi(\mathbf{r}) \leftarrow \chi(\mathbf{r}) + [U_w(\mathbf{r}) - R(\mathbf{r})]/a$ for each $\mathbf{r}$;

(5) Replace each negative value of $\chi(\mathbf{r})$ by 0.

Regularization parameter γ is chosen experimentally with values in the range of about 0.0001 to 1. When the deconvolution converged, i.e. the mean image is changing by less than 1%, we stop the iteration.

A.2 Hippocampal neuron preparation

Primary hippocampal neuron cultures were established through our previously reported protocol [40]. The CA1-CA3 region of hippocampi from postnatal (P1-P2) Long-Evans BluGill rats were removed, enzymatically digested (25.5 U/mL papain, 30 min Worthington Biochemical Corp., Lakewood, NJ), then rinsed, dissociated, and centrifuged (1400 rpm) in supplemented Hibernate-A. Cell pellets were resuspended in Neurobasal-A, counted on a hemacytometer, and plated at 100-125 cells/mm^2 into glass-bottomed Fluorodishes (FD-35, World Precision Instruments, Sarasota, FL). This serum-free media greatly inhibits mitotic cell proliferation; however, in our hands we observe fluorodishes promoting a modest retention of mitotic cells, which we attribute to the Fluorodish. The glass surface demonstrates a robust hydrophobic interaction with low protein containing aqueous solutions. Both Hibernate-A (Brain Bits, Springfield, IL) and Neurobasal-A (Invitrogen) were free of phenol red and were supplemented with 0.5 mM L-glutamine (Invitrogen), B-27 (Invitrogen), 100 U/mL penicillin and 0.1mg mL^{-1} streptomycin (Sigma). Cells were housed in a humidified incubator with 5% CO_2 at 37°C until used; imaging was performed at room temperature unless otherwise specified.

A.3 Immunocytochemistry of cultured neurons

Immunocytochemical labeling of neuronal cultures was performed based on the previously published protocol [40]. Cultures were gently rinsed twice with 2 mL of pre-warmed (37°C) 4% paraformaldehyde in 0.1M phosphate buffered saline (PBS) followed by a 30 min

incubation of 4% paraformaldehyde in PBS on a rotating platform shaker (Gyrotory shaker, model# G76, New Brunswick Scientific). The fixed cells were then permeabilized with 0.25% Triton in PBS for 5-10 min. To block non-specific antibody binding, cultures were incubated with 5% normal goat serum (NGS) or 10% bovine serum albumin in PBS for 30 min. Cells were then labeled by incubating the fixed cultures in primary and secondary antibodies diluted into 2.5% NGS in PBS. Primary antibodies used include: monoclonal anti-α2,8-polysialic acid (PSA) 1° antibody #735 (provided by Rita Gerardy-Schahn, Medizinische Hochschule, Hannover, Germany). Secondary antibodies were goat-anti-mouse Alexa 488 (Invitrogen). Following cell labeling, the fixed cultures were rinsed with PBS and imaged immediately in PBS.

A.4 Movie captions

Movie 1. Depth sectioning through a 3.12 μm polystyrene bead immersed in objective immersion oil (Zeiss immersol 518F, refractive index 1.518). Objective: Zeiss Plan-Apochromat 63 × /1.4 oil.

Movie 2. Comparision between SLIT imaging and confocal microscopy using cultured primary hippocampal neuron. The z-stack used to generate 3D can be seen in Movie 3 for SLIT and Movie 4 for confocal microscopy. Objective for SLIT: Zeiss EC Plan-Neofluar 40 × /0.75; Objective for confocal: Zeiss C-Apochromat 40 × /1.2 water.

Movie 3. Depth sectioning through a hippocampal neuron using SLIT. Depth is indicated in steps of 0.2 μm. Colorbar indicates refractive index. Objective: Zeiss EC Plan-Neofluar 40 × /0.75.

Movie 4. Laser scanning confocal z-stack of a hippocampal neuron cultured for 11 days and stained with antibodies that recognize the polysialic acid post-translational modification on the neural cell adhesion molecules on the extracellular surface. Colorbar indicates fluoresence intensity. Objective: Zeiss C-Apochromat 40 × /1.2 water.

Movie 5. Depth sectioning through a U2OS cell during mitosis. Depth is indicated in steps of 0.2 μm. Colorbar indicates refractive index. Objective: Zeiss EC Plan-Neofluar 40 × /0.75.

Acknowledgements